



High-performance one and two-dimensional doped polypyrrole nanostructure for polymer solar cells applications

Eman M. F. Abd El. Halium^{1,2}, Howaida Mansour^{3,4}, Najah. F. H. Alrasheedi¹, and Ahmed F. Al-Hossainy^{5,6,*}

¹ Chemistry Department, College of Science and Arts, Qassim University, Ar Rass 51921, Saudi Arabia

² Chemistry Department, Faculty of Science, Aswan University, Aswan 81528, Egypt

³ Physics Department, College of Science and Arts, Qassim University, Ar Rass 51921, Saudi Arabia

⁴ Physics Department, Faculty of Women for Arts, Science, and Education, Ain Shams University, Cairo, Egypt

⁵ Chemistry Department, Faculty of Science, Northern Border University, Arar 1321, Saudi Arabia

⁶ Chemistry Department, Faculty of Science, New Valley University, El-Kharga, New Valley 72511, Egypt

Received: 5 January 2022

Accepted: 26 February 2022

Published online:
23 March 2022

© The Author(s), under exclusive licence to Springer Science+Business Media, LLC, part of Springer Nature 2022

ABSTRACT

Hydrochloric acid-doped polypyrrole one and two dimensions have been produced in the existence of methyl orange dye (MO) and sodium dodecyl sulfate (SDS) using ferric chloride (anhydrous) as an oxidizing agent via oxidative polymerization method. Both MO and SDS played an exclusive rule in the preparation of polypyrrole. Using MO produces PPy nanotubes (PPy-M) while using SDS produces sheet form (PPy-S). The use of doped polymer instead of polymer is one of the most critical tasks to improve the electrical conductivity of the fabricated polymer solar cells. The structure of doped polypyrrole was examined by FTIR. Surface morphologies were studied by SEM technique. The thin films of the doped polypyrrole [PPy-S]^{TF} and [PPy-M]^{TF} were fabricated by utilizing the physical vapor deposition (PVD) technique at 5×10^{-5} mbar with a thickness of 150 ± 5 nm/25 °C. The doped polypyrrole thin films were tested by both experimental and, DFT theoretical methods (DMOl³), including FT-IR spectrum and optical properties. The results specifically determine that ΔE_g^{Opt} values and it found up to 2.88 eV and 2.15 eV by the DFT calculations of HOMO and LUMO for [PPy-S] and [PPy-M], respectively. This result indicates that the doped polypyrrole tubes have a conductor property more than [PPy-S]. The heterojunction represents a photo-voltaic performance through $V_{oc} = 0.59V$, $J_{sc} = 4.88$ mA/cm, FF = 0.532 and, $\eta = 4.85$ under illumination neath 50 mW/cm² white-light lighting. The comparison between the one and two-dimensional polypyrrole was achieved based on different parameters.

Address correspondence to E-mail: ahmed73chem@nvu.edu.eg

1 Introduction

Polypyrrole (PPy) is one of the most recognized conducting polymers [1, 2]. This polymer is nontoxic and environmentally stable and evaluated for different applications includes dye-sensitized solar cells [3], corrosion protection of metals [4], absorption of electromagnetic radiation [5], sensors [6], and electrodes in super-capacitors [7]. Recent research on conducting polymers has centered on controlling the morphologies of conducting polymers, particularly at the nanoscale. Nanorods, nanotubes, and nanofibers are examples of one-dimensional structures. Because of their potential applications in energy storage, sensors, electrocatalysis, and electromagnetic interference shields, these morphology forms seem promising. These structures are better for charge transmission than spherical shapes [8]. Polypyrrole (PPy) was effectively produced as a conducting polymers with various surface morphologies, containing particles, nanowires, and nanotubes, using or removing several types of surfactants by a chemical oxidative polymerization process. The findings demonstrate that the surface morphologies of the resultant PPy can be efficiently manipulated and have distinct consequences on their behavior [9]. The conductivity and shape of the resultant polypyrrole are affected by modifying the reaction conditions by changing the acidity, temperature, and adding additives such as surfactants or dyes [10]. Polypyrrole, on the other hand, has been made utilizing a variety of initiators, including ammonium persulfate, hydrogen peroxide, and metal salts. Iron (III) chloride is one of these initiators, and it is a simple and cost-effective procedure that can be done in an aqueous medium, at room temperature, open air, short time, and high conversion rate [11, 12]. The spherical morphology transforms to nanotubes, and nanofibers and, one-dimensional type under particular polymerization circumstances, such as in the presence of certain surfactants [13, 14]. Surfactants aid in the formation of polypyrrole chains into nanotubes or nanowires. During polymerization, the micelles produced by surfactants function as soft templates [15]. Methyl orange dye (MO), which plays a significant role in the production of polypyrrole nanotubes [16], is the most fascinating in-situ-generated template type. When ferric chloride is added to the pyrrole monomer in the presence of methyl orange, ferric ions form needle-like crystals in combination with the methyl orange.

The resulting complex acts as a rigid template for the pyrrole polymerization process. Which pyrrole reduces ferric ions to ferrous ions and then, the generated insoluble ferric complex becomes soluble, and the methyl orange can be incorporated into polypyrrole nanotubes [17–20]. The role of the generated complex is supported by the fact that other oxidants, such as ammonium peroxydisulfate and failed to produce nanotubes [21]. The scattering effect is frequently reduced by directing electron transport along fibers or tubes [22]. electronic devices, polymeric batteries, and functional thin films, among other things, are commercial applications of PPy. Polypyrrole coatings are thermally stable and well suitable for use in carbon composites [23–25]. There are different routes to convert PPy from an insulator form to a conductor form. One of them involves doping PPy with reducing agents, which supplies electrons to the unfilled band of the polymer chains during polymerization process. The oxidative polymerization route was used to prepare doped polypyrrole in one dimension and two dimensions using methyl orange as an in-situ-generated template and SDS as a surfactant. The distinction between these two types was made and used to create polymer solar cells.

2 Experimental step

2.1 Raw materials

Pyrrole monomer, ethyl alcohol, ferric chloride (anhydrous), MO, hydrochloric acid, and sodium dodecyl sulfate (SDS) were purchased analytical grade from Sigma-Aldrich, Steinheim, Germany (99.99%). The reagents were not further purified before use.

2.2 Procedures

Polypyrrole samples were synthesized according to our previous work [26]. A simple chemical oxidative polymerization method was used to prepare PPy samples. 3.5 g methyl orange (MO) and 3.45 g sodium dodecyl-sulfate (SDS) were typically dissolved separately in 100 mL of ethyl alcohol. The solutions were diluted by distilled water up to 400 mL at room temperature using a magnetic stirrer (875 rpm). The solutions' pH was adjusted to 1.6 by

adding few drops of concentrated HCl. Then, for 20 min, 4 mL of pyrrole was added up to the MO and SDS solutions separately under the same conditions. Then, for about 2 h, 160 mL (0.5 M FeCl₃) was added to each solution drop wisely. The resulting obtained HCl doped polypyrrole was stirred with a magnetic stirrer for a further hour. HCl doped polypyrrole that resulted was allowed to settle overnight. To remove the MO or SDS, unreacted monomer, and extra ferric chloride, resulting in ferrous chloride during the reaction, the obtained polypyrrole samples were filtered and washed numerous times by distilled water before being washed with ethanol. The collected polypyrrole samples were dried for two days at 65 degrees Celsius and labeled with [PPy-S] and [PPy-M], respectively.

2.3 Fabrication of the thin films by a PVD technique

A thin film of hydrochloric-doped polypyrrole was created using a physical vapor deposition approach (PVD). Figure 1a, b shows the manufacturing and synthesis process for thin films utilizing the PVD method. The thin films were precipitated on the substrate of a (p-Si) single-crystal wafer and an ITO/glass at 5103 Pa, with interdigitated-electrodes separated by 75 μ. The deposition rate of 3/s was carried out a UNIVEX 250 Leybold, the W-boat tantalum at a rate of 2–3/s through a shadow mask to create a channel with a length and width of 110 m and 1.2 mm, respectively, with a continuous vacuum at all times [27]. The film thickness was 150 ± 5 nm as determined by a quartz-crystal microbalance on a UNIVEX machine. Figure 1a. From the substrate

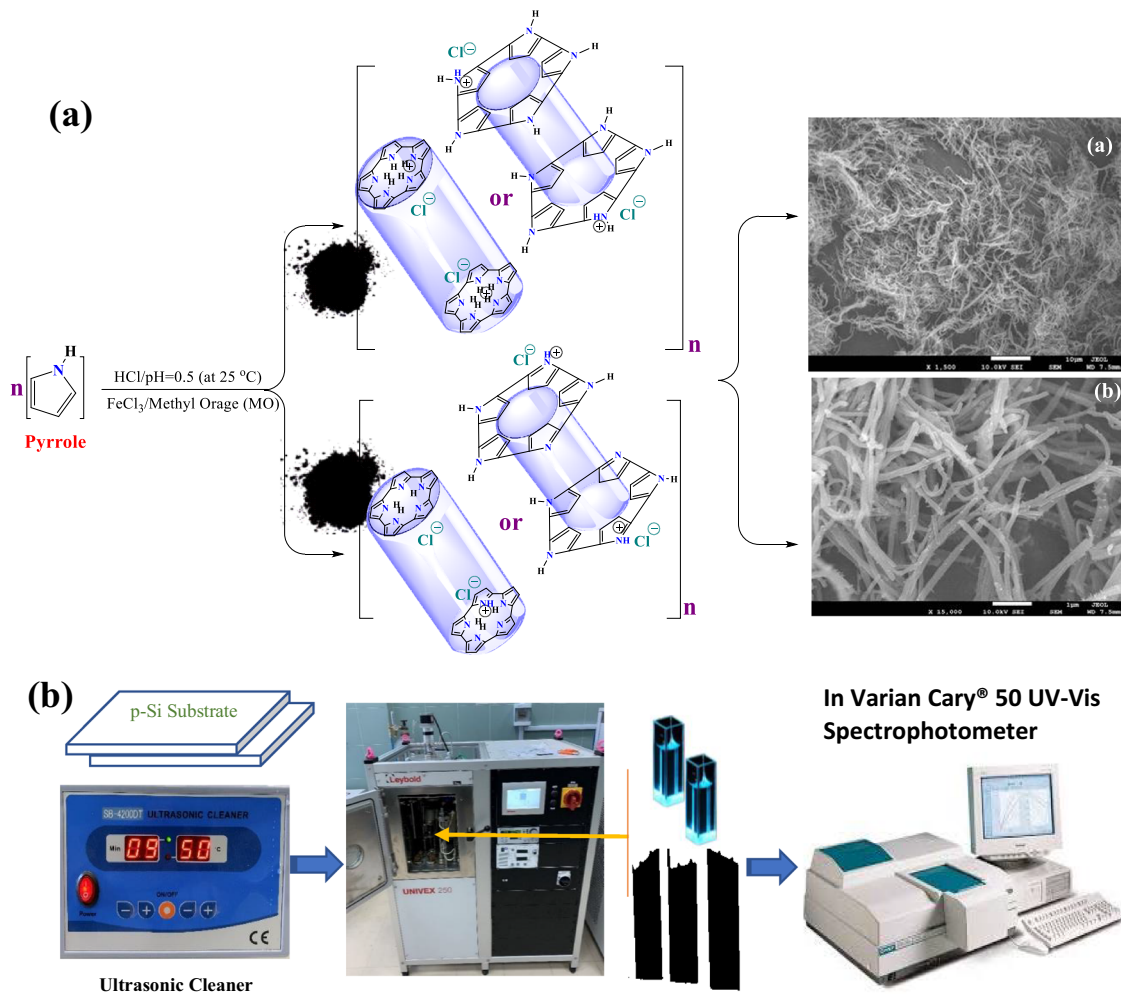


Fig. 1 a, b Synthesis and fabrication scheme for thin films using PVD method

interface to the film surface, There is no reaction between the film and the substrate was noticed [28, 29].

2.4 Computational study

The molecular-structure performance and frequency studies for the [PPy-S]^{TF} isolated molecule in the gas phase were determined using the DMol³ computation. Natural pseudo-positive conservators, functional PBE/GGA association, and a basic DNP set designed for acceptable compounds were all investigated using DMol³ [30]. The entire value of the plane wave power cut off was calculated to be 830 eV. The physical and spectroscopic parameters of an isolated [PPy-S]^{TF} molecule were determined using the IR properties of DMol³, resulting in the GP frequency. Becke's functional connection is also influenced by three elements [31]. The shape and vibrant consistency (IR), [PPy-S]^{TF} in the gas phase, and nanofluids in the gas phase were improved by forming a Lee–Yang–Parr-purposeful (B3LYP) [32] connection with WBX97XD/6-311G. The GAUSSIAN 09 W System researches symmetrical variables, images of arrangements, and the thin film's vibration process complications. The B3LYP method built on WBX97XD/6-311 G has yielded valuable findings for the connection between setup and spectrum reported [33]. The GAP technique was utilized to evaluate the characterizations of Gaussian and DMol3 doped v in isolated molecules, as well as deliberate descriptor alterations and the combined usage of suitable modification with varied complexities [34].

3 Results and discussion

3.1 Combined between the experimental FTIR spectra and Gaussian DFT method

FTIR spectra of the PPy samples are represented in Fig. 2. The following characteristic bands are located at 855, 1035, 1175, 1460, and 1557 cm⁻¹. The peak at 855 cm⁻¹ can be due to C–H wagging, while that at 1035 cm⁻¹ is corresponding to the N–H stretching vibration and C–H in-plane deformation. The C–N stretching vibration mode in the PPy five membered ring is responsible for the following two bands, which are positioned at 1175 and 1460 cm⁻¹,

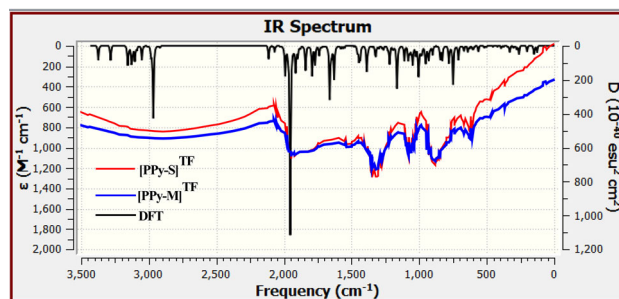


Fig. 2 FTIR of experimental and theoretical polypyrrole

respectively, whereas the symmetric ring vibration of C–C bonding is responsible for the band at 1557 cm⁻¹ [35]. The theoretical FTIR spectrum, on the other hand, was approximated using the isolated molecule's spectroscopic indications. Figure 2 depicts the modest differences between evaluated frequencies and the expected. The primary distinction is that the count was performed in a vacuum, whereas the calculations were calibrated in a solid state. Because the polymer's vibrational modes are complex, low symmetry results, and it's tough to attribute torsion as well as all plane modes because ring modes degenerate alongside imitative ones. However, the graph shows some noteworthy changes [36]. The following equation for [PPy-S] shows the direct association between computed ($\lambda_{\text{Cal.}}$) and experimental wavenumbers ($\lambda_{\text{Exp.}}$) Polypyrrole. $\lambda_{\text{Cal.}} = 0.961 \lambda_{\text{Exp.}} + 10.13$ with correlation coefficient ($R^2 = 0.99$). For [PPy-S] polymers: $\lambda_{\text{Cal.}} = 0.957 \lambda_{\text{Exp.}} + 15.08$ with correlation coefficients ($R^2 = 0.999$).

3.2 SEM of [PPy]^{TF}

Nanotubes frequently have different features than the standard spherical shape, which is why one-dimensional morphology is of great interest in both basic and practical science. Polypyrrole's ability to self-organize into forms with specified morphology and characteristics suggests that its molecular and macromolecular structure is highly defined and that it is not simply a combination of diverse oxidation products. MO is employed as an in-situ produced template for the production of doped polypyrrole tubes, and methyl orange has played a unique role in the fabrication of polypyrrole nanotubes. The properties of nanotubes depend on the concentrations of pyrrole, ferric chloride, and methyl orange, and medium solvent [37, 38]. Figure 3a, b shows tubes

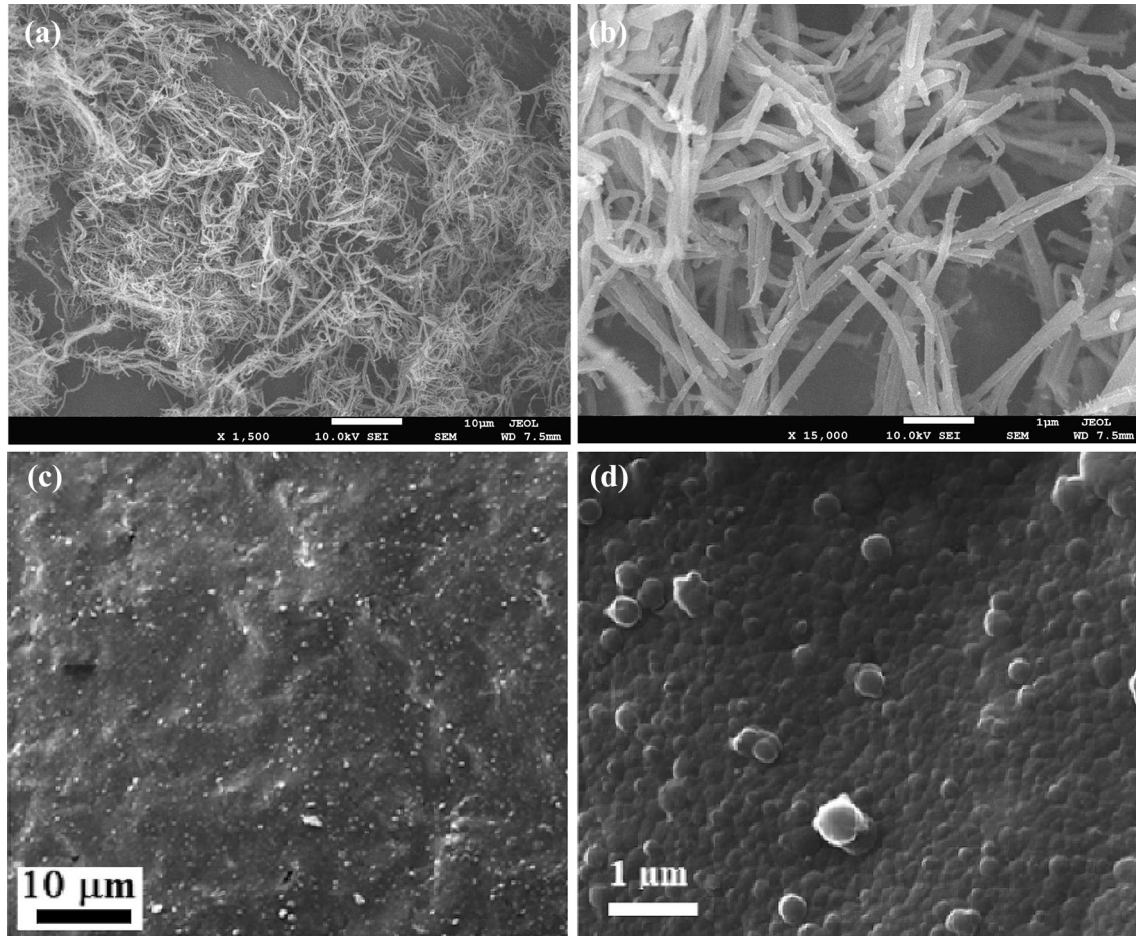


Fig. 3 a, b SEM images for [PPy-M] and c, d [PPy-S] at two different magnifications

form clearly in agreement with Kopecká et al. [37]. Figure 3c, d) displays a sheet form clearly of PPy-M with uniform particles in two dimensions.

SDS plays an important role as a soft surfactant during the polymerization process at the considered condition of the experiment. This confirms that the surface morphology of the resulting polypyrrole depends on the organic compound used during the polymerization process. With alternating the organic compound types and conditions of the experiment, the resulting surface morphology also varies. The difference in the surface morphology and physical properties of the resulting polypyrrole depends on the surfactant types, which are used. MO produces one-dimensional- PPy-M (nanotubes Fig. 3a, b) while SDS produces two-dimensional-PPy-S (sheet Fig. 3c, d).

3.3 Combined between the experimental XRD and Gaussian DFT method

[PPy-S]^{TF} and [PPy-M]^{TF} phases were observed within the instrumental sensitivity, as shown in Fig. 4. The XRD pattern obtained from the fabricated [PPy-S]^{TF} is amorphous, with one peak appearing at

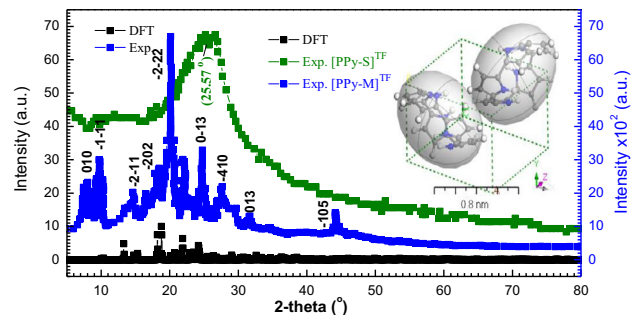


Fig. 4 Combined between the experimental ([PPy-S]^{TF} and [PPy-M]^{TF}) and simulated PPy-S XRD patterns, inset Fig. 3D Triclinic (polymorph computation method)

Table 1 The results of the [PPy-S] program Refine Version 3.0 Software Program (Kurt Barthelme's & Bob Downs)

Symmetry	Experiential			Calculated		difference		FWHM	D_{av}^b
	2θ	d	hkl	2θ	d	2θ	d		
[PPy-S] ^{TF}	7.589	11.46	010	7.6017	11.43	0.012	0.018	1.7701	71.15
Triclinic (\bar{P}_1)	9.728	8.976	– 1 to 11	9.9092	8.811	0.184	0.164	0.1376	62.50
$a = 9.19(3)$; $b = 9.8(1)$	14.69	5.975	– 2 to 11	14.6841	5.978	– 0.007	– 0.00	0.6676	47.25
and $c = 9.02(3)$ nm	18.45	4.774	– 202	18.4253	4.780	– 0.022	– 0.05	0.8608	48.25
$\alpha = 59.9(5)^\circ$; $\gamma = 110.9(3)^\circ$	20.03	4.402	– 2 to 22	20.0173	4.405	– 0.016	– 0.03	1.1312	89.70
$\beta = 105.9(4)^\circ$	24.77	3.574	0–13	24.7537	3.576	– 0.015	– 0.02	0.4563	95.26
$V = 700$ (7); Rmse ^a = 0.046	27.59	3.215	– 410	27.5998	3.215	0.003	0.003	1.7831	77.16
$\lambda = 1.541838$ Å	31.70	2.809	013	31.6924	2.810	– 0.007	– 0.06	0.0242	97.25
ME ^c = – 0.053	44.27	2.038	– 105	44.279	2.038	0.0066	0.002	0.7201	39.56
Average									69.79

^aRoot mean square error^bnm^cMachine error

$2\theta = 25.57^\circ$. On the other hand, The XRD pattern obtained fabricated [PPy-S]^{TF} had correlated to the isolated system matrix. The predicted crystallite size (D) and miller indices (hkl) are both dependent on the full width at half-maximum (FWHM) values, as given in Table 1. The code data basis are cod_database_code 1007186 and database_code_amcsd 0012305 agrees well with the interplanar distances d-spacing [39]. To denote peak lines studied by diffraction that are close to the results obtained, the TDDFT-DFT and Crystal Sleuth-Microsoft programs are employed [40]. The Debye–Scherrer was applied to measured XRD for [PPy-S]^{TF}, the range of $5 \leq 2\theta \leq 45$ with $1/dhkl = 0.0566 \text{ \AA}^{-1} - 0.7446 \text{ \AA}^{-1}$, $\lambda = 1.540562 \text{ \AA}$, $I_2/I_1 = 0.5$, polarization = 0.5, and function Pesedo-Voigt. From Scherer's formula, $D = 0.9 \lambda / (FWHM \cdot \cos\theta)$, where λ is the X-ray wavelength (1.541838 Å). The produced [PPy-S]^{TF} XRD data from the XRD pattern was utilized to examine variables and features such FWHM, crystallite size, hkl indices, d-spacing (d), and peak intensity, as shown in Table 1. Between 39.56 and 97.25 nm, the crystalline size was $D_{av} = 69.79$ nm. The theoretical X-ray diffraction models (version 7.0) were calculated by Polymorph using content studio software (see Fig. 4). The integrals were performed on the Brillouin zone with $2 \times 2 \times 1$ inset Fig. 4. (Polymorph [PPy-S]^{TF}). For [PPy-S]^{TF}, Between experimental X-ray structures and observed PXRD patterns, an experimental comparison was done. While the intensity

and location of specific peaks differ significantly between experimental and PXRD models, the emphasis here is on their general closeness. As a result, only the most essential comparison qualities between the measured and experimental data should be assessed. Instrumentation and data collection techniques are just two of the many factors that can influence the experimental PXRD pattern. The simulated [PPy-S]^{TF} in polycrystalline as an isolated position and offer a Triclinic in the group \bar{P}_1 . A thorough examination of the computed and experimental PXRD patterns for [PPy-S]^{TF}, demonstrating good agreement and supporting the PXRD patterns' accuracy. As demonstrated in Fig. 4, combining physically based diffraction with density functional theory calculations yields a reasonable estimate of the atomic scale for [PPy-S]^{TF} (2θ at hkl ($\bar{2}22$)).

3.4 Geometry study and molecular electrostatic potential (MEP)

Before implementing modeling for isolated molecules [PPy-S]^{TF} and [PPy-M]^{TF} films, many statements on the influence of positive and negative surface ratios on electron levels were studied. The difference in the average field, as well as the negative and positive regions, for a sample of over 1000 electron density molecules. The results suggest an average 15% reduction in the total when MEPs are related with 0.01–0.002 au. The data also show that until a certain

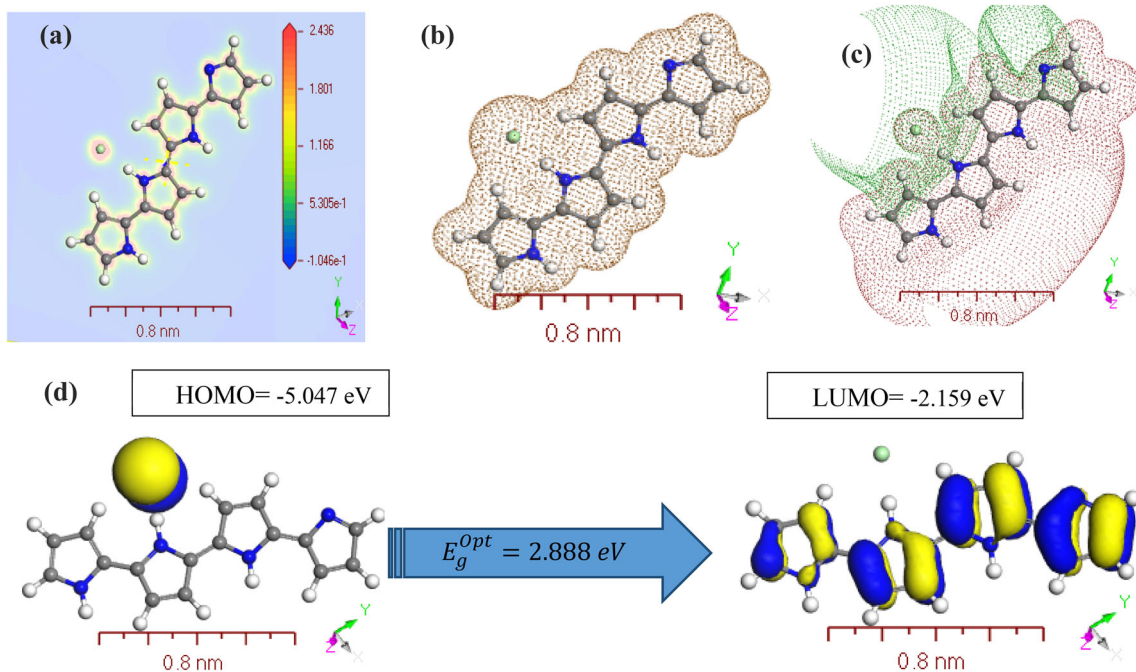


Fig. 5 DFT computation of **a** MEP of the [PPy-S], **b** Electron density of the [PPy-S], **c** Potentials of the [PPy-S], and **d** DFT computation for HOMO and LUMO calculations of the [PPy-S] using the DMOI³ method

number of nuclear nuclei is reached, the positive surface density value remains constant while the number of negative sections decreases. 09 w/DFT Gaussian [41, 42]. At 0.002 au, the positive area percentage is roughly 68%; at 0.01 au, it is over 85%. Visual representations of the MEP Iso-surface value of -15 kcal/mol may be employed in nanofluid pairs of fields [43, 44], as shown in Figs. 5a and 6a. The estimated MEPVmin 3D minimum values nearest to the lone pair region of both polymers are -1.0461×10^{-1} and -9.907×10^{-1} kcal/mol, respectively, for the [PPy-S]^{TF} and [PPy-M]^{TF} is given by MEP's topography. Using DMOI3/DFT designs,

the established nanofluids MEPVmax values for the [PPy-S]^{TF} and [PPy-M]^{TF} are 2.436 and 1.685×10^{-1} kcal/mol, respectively. As predicted, the estimated MEP Vmax and MEP Vmim will take into account the presence of the electronic alternative. The robust electron life of his unusual partnership is reliant on nanofluid-donating replenished energy. In the lonely pair zone, the MEP Vmim value provides a simple way to define pair power. As an example, a copolymer with a donor engine. The negative MEP Vmimrange's key feature is that it raises the electron density in a single pair of nitrogen atoms. To lower the unfavorable life of MEP Vmim, an electron pull

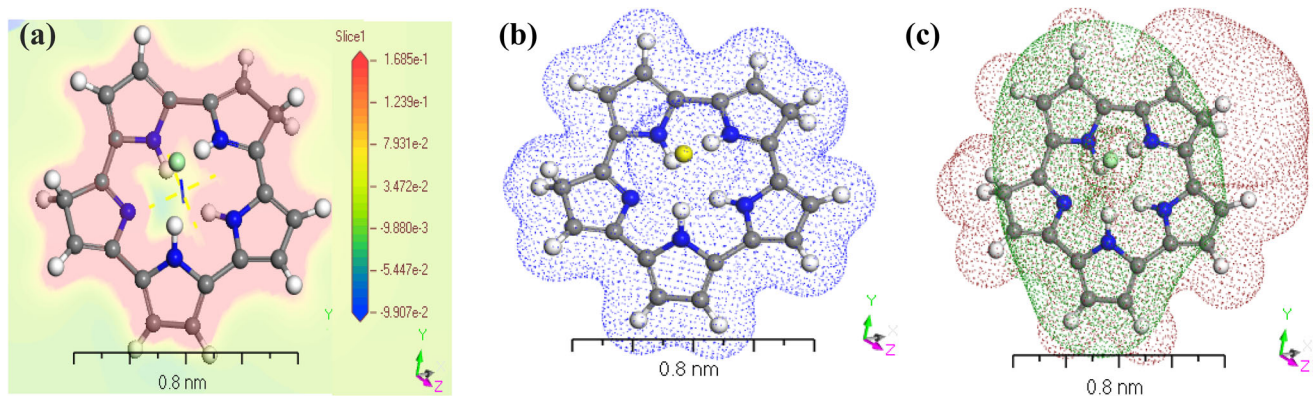


Fig. 6 DMOI3 technique of **a** MEP of the [PPy-M]; **b** Electron density of the [PPy-M]; and **c** Potentials of the [PPy-M]

out of the cluster is also required. MEP Vmim focused on nanofluid electrical impact calculations, which might be more practical and transparent than structures based on a variety of values (NH). The polymer matrix-donating strength is employed in the imagining [PPy-S]^{TF} and [PPy-M]^{TF}. The energy exchange between [PPy-S]^{TF} and [PPy-M]^{TF} is entirely equal to the quantity of MEP Vmim [45], when nanofluid movement is not required. Figures 5b and 6b illustrate the electron density in [PPy-S]^{TF} and DNP base sets [PPy-M]^{TF}, 4.4 base file, 0.2 DIIS/magnitude density blend, 5 to 3 ha smearing, respectively. The macro-cyclical plane's negative electrostatic potential is symmetrically distinct in all computations [46], and the geometry of the positive and mutually negative sections differs per base group. Figures 5c and 6c show how the source range (DNP) is stretched to DN and then irrelevantly further extended with base folder (4.4), SCF lenience (0.0001), and maxi.

In global reactivity descriptors based on quantum predictions, the highest occupied molecular orbit (HOMO) and the lowest unoccupied molecular orbit (LUMO), depicted in Figs. 5d and 6d, are substantially standard [47, 48]. The molecule's equilibrium is determined by the difference in energy between FMOs, which is significant in estimating electrical conductivity and comprehending electricity transport. The presence of fully negative EH and EL values indicates that the isolated chemicals are stable [49, 50]. The measured FMOs are used to calculate the electrophilic sites of aromatic compounds. On the M–L sites, the Gutmannat variance approach was utilized to boost EH when M–L bonds expanded and bond length decreased [51]. The energy gap, kinetic stability of the molecule, and the chemical reactivity under study were shown using E_g^{Opt} [52, 53]. Softness and hardness are the most critical factors in determining stability and reactivity [54, 55]. The operational formula $(\epsilon_H + \epsilon_L/2)$ has been given in the single-electron energy field of boundary molecular orbital HOMO (ϵ_H) and LUMO (ϵ_L), as described in Table 4. The energy bandgap, which describes the relationship of charge transport within the molecule, can also be seen on the same table. The highest-valued molecular orbital coefficients define the coordination position. As shown in Table, this is the oxygen of the C–N–H group. The HOMO level is frequently found on the –C=C–(2), –C=N, and N–H(4) atoms,

which are prime targets for nucleophilic attack. The energy gaps shown in Figs. 5d and 6d are 2.888 and 1.502 eV, respectively, which is an extremely large value for [PPy-S]^{TF} and [PPy-M]^{TF}. This reveals high excitation energies and, as a result, high stability for [PPy-M]. The lower E_g^{Opt} for [PPy-M]^{TF} than for [PPy-S]^{TF} can be attributed to the more polarizable and softer. Soft molecules are referred to as reactive molecules rather than hard molecules since they can provide electrons to an acceptor. The index electrophilicity (ω) of the quantified chemicals is the most intriguing characteristic. The device promises energy stability as it absorbs external electronic charges [56, 57].

3.5 Optical properties

Based on the experimental results of reflectance $R(\lambda)$ and absorbance Abs. (λ), the transmittance T percent (λ) and extinction coefficient $k(\lambda)$ of thin films were calculated using the formula $(T\%(\lambda) = (1 - R(\lambda))^2 \times \text{Exp}(-\text{Abs.}))$ [58, 59]. The absorption coefficient is calculated using the equation = $\text{Abs.}/d$, where d is the observed values of the film thicknesses, as shown in Table 3. Figure 7a illustrates the wavelength (λ) relationship of the transmittance $T\%(\lambda)$ for [PPy-S]^{TF} and [PPy-M]^{TF} films. In region $350 \text{ nm} \leq \lambda \leq 600 \text{ nm}$, the new absorption band has existed at 433 nm and 473 nm assigned to π – π^* electronic transitions for [PPy-S]^{TF} and [PPy-M]^{TF} films. Furthermore, these findings suggest that the formation of [PPy-M]^{TF} can effectively control the optical properties of [PPy-S]^{TF} [60]. Figure 7b demonstrates the dependence of theoretical calculations (TDDFT) of absorbance (Abs.) and wavelength spectra (λ) of the [PPy-S] and [PPy-M] as an isolated molecule in a gaseous state. The absorption of pure [PPy-M]^{TF} is higher than that of the [PPy-S]^{TF} as an isolated molecule in a gaseous state. When the area of absorption and curve behavior of [PPy-S]^{TF} and [PPy-M]^{TF} as isolated molecules in a gaseous state are compared to the λ_{max} values obtained from the experimental approach and TDDFT/DMOI³ calculations, it is clear that there is good agreement in most of the wavelengths considered [61, 62].

The E_g^{Opt} values of [PPy-S]^{TF} and [PPy-M]^{TF} films are determined utilizing Tuac' equation: $(\alpha h\nu)^m = \beta(h\nu - E_g^{\text{Opt}})$, where $h\nu$ is incident photons energy and $m = 1/2$ for indirect and 2 for direct

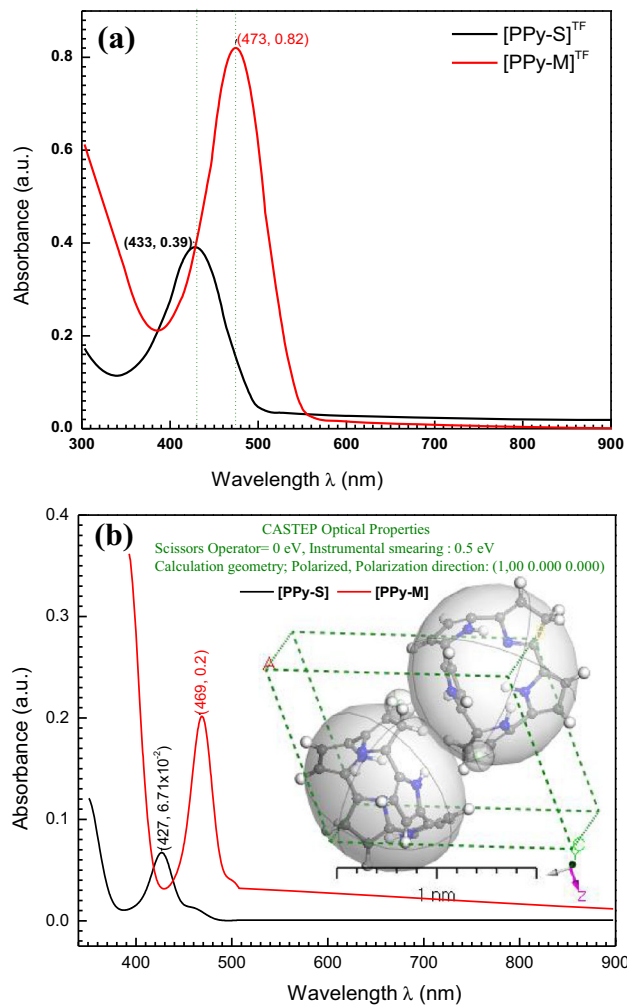


Fig. 7 **a** The absorbance spectra of [PPy-S]^{TF} and [PPy-M]^{TF} thin films (Experimental part). **b** TDDFT/DMO1³ calculation of [PPy-S]^{TF} and [PPy-M]^{TF} in a gaseous state, inset figure is 3D molecule of [PPy-M]^{TF}

allowed transitions. E_g^{Opt} is calculated by extrapolating the straight portion of the $(\alpha hv)^2$ against (hv) plot to the energy axis at $a = 0$ and assuming direct transitions between the valence band and the conduction band in [PPy-S]^{TF} and [PPy-M]^{TF} films (Fig. 8). The direct E_g^{Opt} value for [PPy-S]^{TF} and [PPy-M]^{TF} films are 2.40 eV and 2.16 which is consistent with the informed values for [PPy-S]^{TF} films in the literature [63].

The analysis of the manufactured films' direct and indirect optical band gaps is shown in Fig. 8. Both $(\alpha hv)^2$ and $(\alpha hv)^{0.5}$ have a linear dependence at higher (hv) , as seen in Fig. 8, indicating that both optical transitions are possible for these manufactured films. The optical band gaps, E_g^{Opt} (direct) and E_g^{Opt}

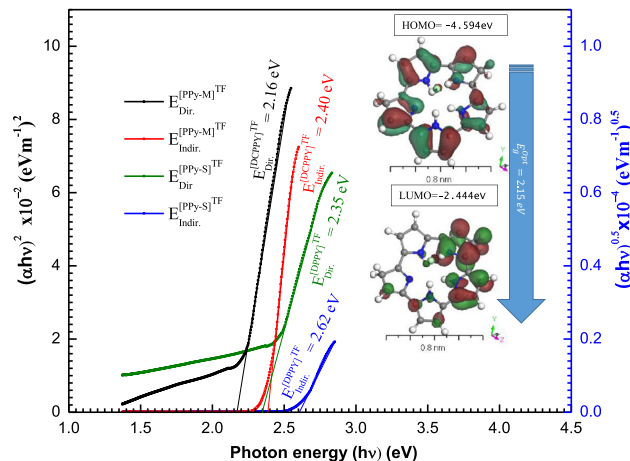


Fig. 8 The relationship photon energy with both $(\alpha hv)^{0.5}$ and $(\alpha hv)^2$ of [PPy-S]^{TF} and [PPy-M]^{TF} thin films

(indirect), are computed by extrapolating the straight-line parts of the curves to zero, and the calculated values are shown in Table 2. E_g^{Opt} (direct) of [PPy-S]^{TF} is 2.35 eV, which lowers to 2.16 eV after the creation of [PPy-M]^{TF}, as shown in Fig. 8 and Table 2 [64].

The combination of [PPy-S]^{TF} with the same another molecule may push energy levels inside the bandgap of [PPy-S]^{TF}, leading to the contraction of its E_g^{Opt} . The same performance is also examined for E_g^{Opt} (indirect) which decreases from 2.62 to 2.40 eV. The film thickness (d), optical properties of [PPy-S]^{TF} and [PPy-M]^{TF} thin films: Optical band gap E_g^{Opt} indirect, E_g^{Opt} direct, refractive index (n) has been tabulated in Table 3.

HOMO and LUMO are key factors in quantum chemical simulations for the complexes analysis known as the boundary molecular orbitals in the molecular orbit (FMOs) for TDDFT/DMO1³ computations (insert Fig. 8). The computed energy E_H , E_L and ΔE_g^{Opt} are presented in Table 4. The tabulated values of all these parameters were calculated using the following equations ($\mu = E_H + E_L/2$), ($\eta = E_H - E_L/2$), ($\chi = -\mu$), ($S = 1/2\eta$), ($\omega = \mu/2\eta$), ($\sigma = 1/\eta$) and ($\Delta N_{max} = -\mu/\eta$), respectively [65, 66]. The negative values of E_{HOMO} and E_{LUMO} energies can be ascribed to product stability for [PPy-S] and [PPy-M] as a matrix for isolated compounds. For the largest magnitude molecular orbital coefficients, coordination position simulation was used. A crucial quantum chemical property is the electrophilicity

Table 2 Calculated ϵ_{HOMO} , ϵ_{LUMO} , electronegativity (χ), chemical potential (μ), global hardness (η), global softness (S), and global electrophilicity index (ω), ΔN_{max} and σ for the [PPy-S]^{TF} and [PPy-M]^{TF} polymers

Compound	E_H	E_L	$(E_H - E_L)$	χ	μ	η	S	ω	$D_{N_{\text{max}}}$	σ
[PPy-S]	- 5.047	- 2.159	- 2.888	3.603	- 3.60	1.444	0.34626	4.49502	2.49515	0.69252
[PPy-M]	- 4.596	- 3.094	- 1.502	3.845	- 3.85	0.751	0.66578	9.84289	5.11984	1.33156

Table 3 Optical properties of [PPy-S]^{TF} and [PPy-M]^{TF} thin films thin films

Films	E_g^{Opt} (eV)		(Refractive Index)		Dielectric constants		Optical conductivity	
	Ind	Dir	$n(\lambda)$	$k(\lambda)$	ϵ_1	ϵ_2	σ_1	σ_2
[PPy-S]TF	2.62	2.35	1.48a	5.35×10^{-9a}	2.19	1.58×10^{-8}	6.14×10^{-6}	1.41×10^{-5}
[PPy-M]TF	2.40	2.16	1.62b	1.24×10^{-8b}	2.63	$4.0.03 \times 10^{-8}$	8.41×10^3	2.15×10^3

^aAt ($h\nu$)= 2.88 eV

^bAt ($h\nu$)= 2.61 eV

Table 4 Geometry constant for [PPy-S] and [PPy-M] as isolated molecules

Compounds	E_H	E_L	ΔE_g	χ	μ	η	S	ω	ΔN_{max}	δ
[PPy-S]	- 5.05	- 2.16	2.888	- 6436.85	- 3220.807	4.765	3.603	- 3.603	- 1.444	- 0.346
[PPy-M]	- 4.59	- 2.44	2.15	- 9473.80	- 4738.641	3.48	3.519	- 3.519	- 1.075	- 0.465

index (t), which analyzes energy stability when the device gets an extra electronic charge [67, 68].

The values of $E_g = 2.88\text{eV}$ and 2.15 eV for TDDFT/DMO³ computations (Inset Fig. 8) were determined by applying the DMol³ procedure in DFT based on the disagreement between HOMO and LUMO for [PPy-S] and [PPy-M] [69]. The simulation results utilizing DFT/DMO³ and experimental data (Tauc's equation) are very similar. Electrical and energy transfer methods can be efficiently evaluated using the data received from two approaches [70].

3.6 The optical constants and refractive index of the films

The absorbance (Abs.), and the reflectance $R(\lambda)$ were evaluated to establish the refractive index $n(\lambda)$ and some dispersion factors. The reflectance is calculated using the formula $R(\lambda) = (n - 1)^2 + k^2 / (n + 1)^2 + k^2$.

Thus, the computed refractive index is $n(\lambda) = (1 + R) + \sqrt{4R - (1 - R)^2 k^2} / (1 - R)$ [71]. Figure 9a

demonstrates the $n(\lambda)$ distributions of the fabricated thin films. The calculated $k(\lambda)$ and $n(\lambda)$ at $h\nu = 2.88\text{ eV}$ and 2.61 eV are tabulated in Table 2. It is noted that $n(\lambda)$ increases from $n(\lambda) = 1.48$ for [PPy-S] to $n(\lambda) = 1.62$ for [PPy-M], it increases with increasing the $h\nu = 2.61\text{ eV}$ till reach 2.88 eV . Similarly, the $k(\lambda)$ increases from $k(\lambda) = 3.53 \times 10^{-9}$ for [PPy-S]^{TF} to $k(\lambda) = 1.24 \times 10^{-8}$ for [PPy-M], it increases with increasing the $h\nu = 2.88\text{ eV}$ till reach 1.24×10^{-8} . It has been determined that when incident light interacts with a material containing many particles, the refraction increases, and, as a result, the refractivity of the films increases [72]. From the behavior of [PPy-S] and [PPy-M] in Fig. 9b, the intensity of four peaks observed are increased with a formation of sheet [PPy-S]. The CASTEP/DFT computations were used to evaluate $n(\lambda)$ and $k(\lambda)$ values from the behavior of the simulated nanocomposite [PPy-S] and [PPy-M] as the isolated state in Fig. 9b, and when compared to the experimental values, the simulated values are close to those achieved by DFT with the CASTEP model [73].

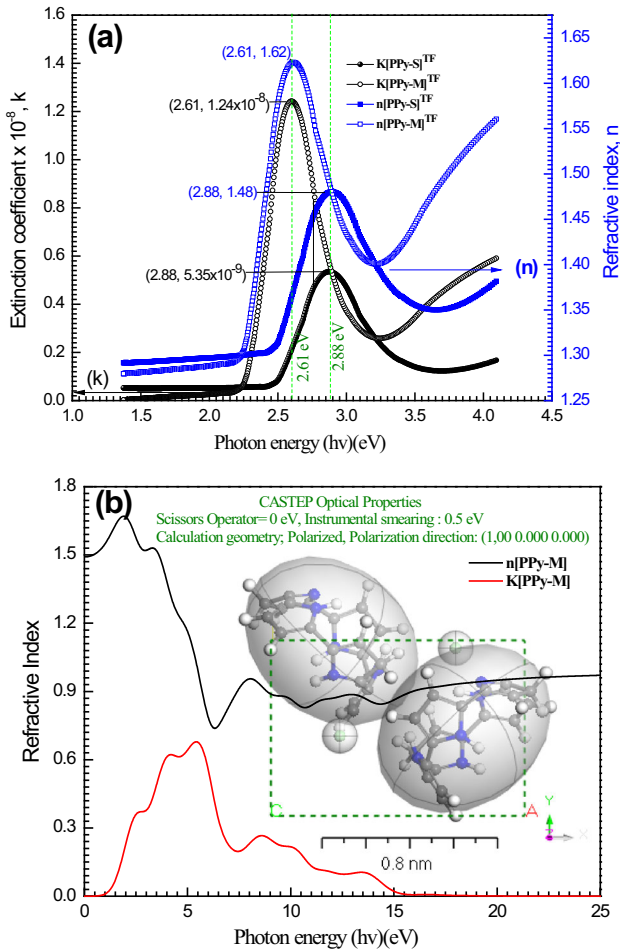


Fig. 9 **a** Plot (*n*) and (*k*) vs photon energy (*hν*) eV for [PPy-S]^{TF} and [PPy-M]^{TF}, **b** The simulated computation of (*n*) and (*k*) for [PPy-M] as isolated molecule by CASTEP/DFT and inset Fig. 3D Triclinic lattice type (polymorph computation method)

The frequency dependence of the optical dielectric constant is a parameter that provides information about the electronic excitations within the material. The real (ϵ_1) and imaginary (ϵ_2) parts were determined by the following equations: $\epsilon_1 = n(\lambda)^2 - k(\lambda)^2$ and $\epsilon_2 = 2n(\lambda)k(\lambda)$ [74]. It is seen, from Fig. 10a, that with increasing photon energy, the ϵ_1 and ϵ_2 values increase and then increase at the higher values of photon energy ($h\nu = 1.50$ eV and 4 eV). The maximum values of ϵ_1 are 2.19 and 2.63 at $h\nu = 2.88$ eV and 2.61 eV for the [PPy-S]^{TF} and [PPy-M]^{TF} thin films. Using the CASTEP technique, the maximum value of $\epsilon_1(\lambda)$ and $\epsilon_2(\lambda)$ for [PPy-S]^{TF} and [PPy-M]^{TF} in isolate state is 0–3 at various frequencies (eV) \cong 0–25, respectively (Fig. 10b). The experimental and simulation dimensions' average values $\epsilon_1(\lambda)$ and $\epsilon_2(\lambda)$ are discovered within the frequency range values of

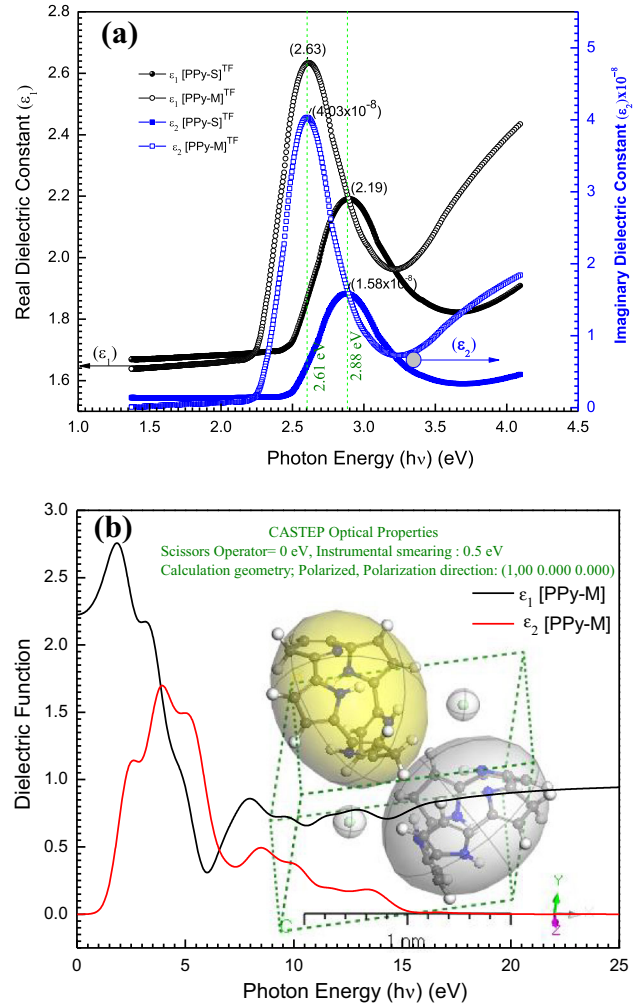


Fig. 10 **a** (ϵ_1 and ϵ_2) vs (*hν*) eV for [PPy-S]^{TF} and [PPy-M]^{TF} thin films. **b** Simulation dielectric function for [PPy-M] as an isolated state by CASTEP method

1–6 eV [75]. As indicated in this figure of [PPy-S]^{TF} and [PPy-M]^{TF}, one peak in the dielectric constant parts performance was detected. The CASTEP/DFT computations were used to evaluate $\epsilon_1(\lambda)$ and $\epsilon_2(\lambda)$ values from the behavior of the simulated composite [PPy-S]^{TF} and [PPy-M]^{TF} as an isolated state in Fig. 10b, and compared to the experimental values for [PPy-S]^{TF} and [PPy-M]^{TF}, simulated values are close to those achieved by DFT with the CASTEP model.

$\epsilon_1(\lambda)$ and $\epsilon_2(\lambda)$ must be mixed according to the following relationship to generate the conductivity spectrum:

$$\sigma \times (\lambda) = \sigma_1(\lambda) + \sigma_2(\lambda); \sigma_1(\lambda) = \omega \epsilon_2(\lambda) \epsilon_0 \text{ and } \sigma_2(\lambda) = \omega \epsilon_1(\lambda) \epsilon_0, \text{ optical-conductivity fragments, } (\omega) \text{ and } (\epsilon_0), \text{ respectively, the frequency of angular and dielectric-}$$

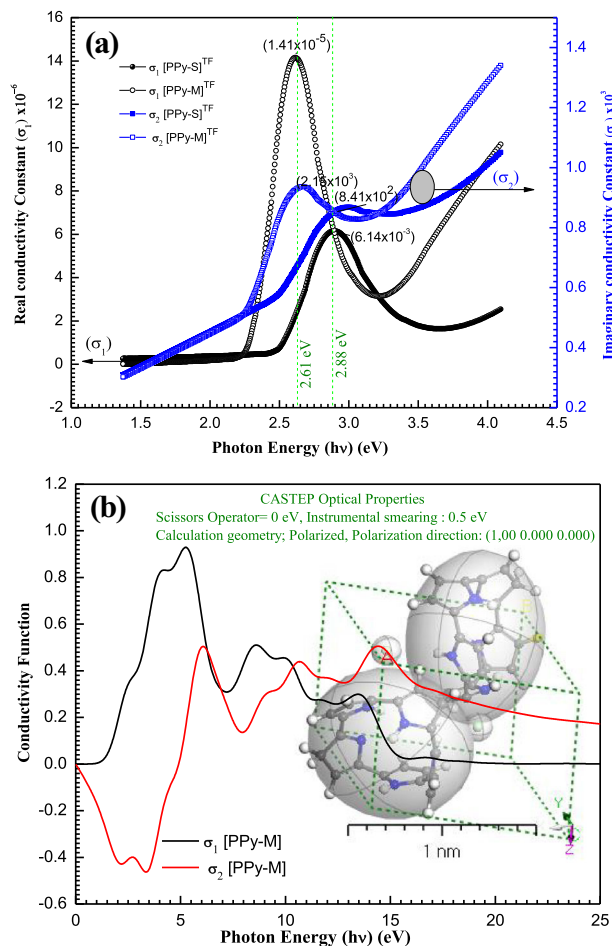


Fig. 11 a σ_1 & σ_2 with ($h\nu$) eV for [PPy-S]^{TF} and [PPy-M]^{TF} thin films. b Simulation conductivity function for isolated state of [PPy-M] by CASTEP method

free space constants [76]. Figure 11a shows the optical-conductivity (real and imaginary portions) of [PPy-S]^{TF} and [PPy-M]^{TF}. The value of σ_2 is higher than the value of σ_1 . For [PPy-S]^{TF} and [PPy-M]^{TF}, in the experimental-part (Fig. 11a), the $\sigma_1(\lambda)$ showed the maximum values of 6.14×10^{-6} , and $1.41 \times 10^{-5} / \Omega/\text{m}$ at the photon energy value of 2.61 and 2.88 eV, respectively [77]. The $\sigma_2(\lambda)$ gives the maximum values of 8.41×10^3 and $2.51 \times 10^3 / \Omega/\text{m}$ for [PPy-S]^{TF} and [PPy-M]^{TF} at the same photon energy value of $\sigma_1(\lambda)$, respectively. The high value of the calculated ratio $\sigma_1(\lambda)/\sigma_2(\lambda) = 7.30 \times 10^{-10}$ indicates that σ_2 is dominated [78]. The $\sigma_1(\lambda)$ and $\sigma_2(\lambda)$ of the [PPy-S]^{TF} and [PPy-M]^{TF} as isolate state depends on ($h\nu$) are validated in insert Fig. 11b. In the CASTEP technique, for [PPy-S]^{TF} and [PPy-M]^{TF}, the maximum values of $\sigma_1(\lambda)$ and $\sigma_2(\lambda)$ are (1.40 Ω/m , 5.96 eV) for the $\sigma_1(\lambda)_{[DCPPy]}$. For $\sigma_1(\lambda)$ and $\sigma_2(\lambda)$, the experimental

method and the CASTEP technique produced similar findings.

3.7 Fluorescence studies

The fluorescence emission and excitation spectra of [PPy-S]^{TF} and [PPy-M]^{TF} are depicted in Fig. 12a, b. Fluorescence emission peaks were examined at 557 nm and 594 nm for [PPy-S]^{TF} and [PPy-M]^{TF}, respectively. The observed Stokes shift, $\Delta = \lambda_{\text{Emission}} - \lambda_{\text{Excitation}}$, was computed as $\cong 25$ nm and 31 nm, for [PPy-S]^{TF} and [PPy-M]^{TF}, respectively. The excitation and absorption spectra are comparable, and both shapes are mirror reflections of one another. When compared to the absorption spectra, the excitation spectrum was a little red-shifted in terms of wavelength.

Figure 12c illustrates a Commission Internationale de l'Eclairage (CIE) graphs of the emission colors of powders and different solution concentrations, as well as digital photographs obtained under UV light at $\lambda_{\text{max}} = 557$ nm and $\lambda_{\text{max}} = 594$ nm for [PPy-S]^{TF} and [PPy-M]^{TF}. All of the fabricated thin film and solutions emitted a deep-blue light with a CIE of $y < 0.1$. As a result, the researched manufactured polymers may be classified as crucial luminous since they emit white-light from a single material and deep-blue light from their solutions [79].

3.8 Photovoltaic properties of the Au/[PPy-S]^{TF}/n-Si/Al and Au/[PPy-M]^{TF}/n-Si/Al structure

Figures 13a, b demonstrate the illuminated $I-V$ characteristics of Au/[PPy-S]^{TF}/n-Si/Al and Au/[PPy-M]^{TF}/n-Si/Al heterojunctions. In the light, the current value of this device at a given voltage is higher than in the dark. This means that light absorption by the active layer creates excitons, which then dissociate into free charge carriers at the barrier, contributing to the photocurrent. The [PPy-S]^{TF}-Si and [PPy-M]^{TF}-Si interfaces, specifically. On the contrary way, light illumination has been discovered to dramatically boost the photocurrent in the device. This pattern offers vital information about the electron-hole pairs generated by incoming photons in the junction. Along the potential barrier at the interface, the electric field at the junction directed-free electrons and holes towards the electrodes. As demonstrated in Fig. 13, the device possesses photovoltaic qualities,

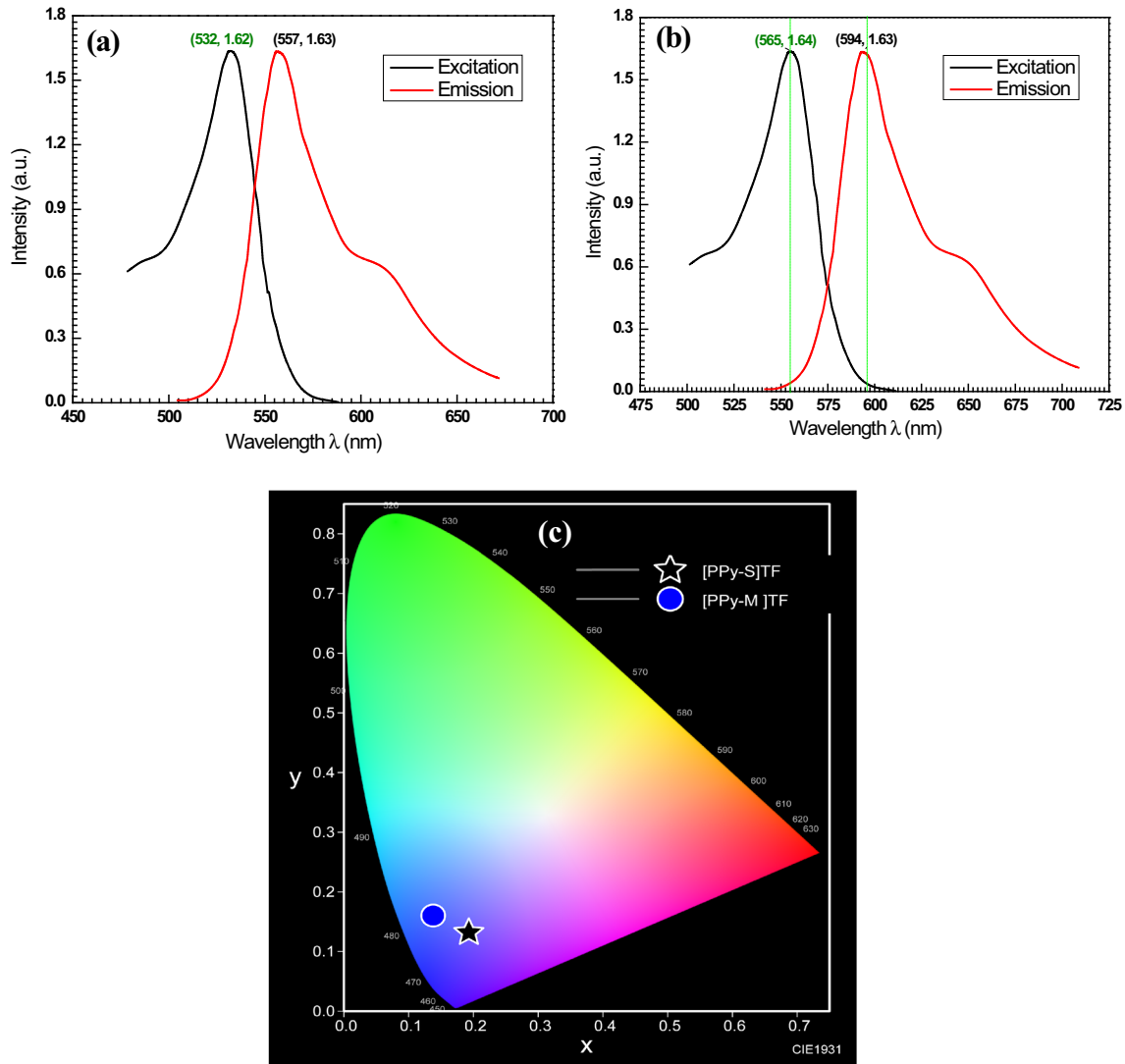


Fig. 12 Excitation-emission spectra of **a** [PPY-S]^{TF}; **b** [PPY-M]^{TF} films and **c** at 298 K

with a high short-circuit photocurrent density (J_{sc}) of $4.88 \times 10^{-3} \text{ A/cm}^2$ [80, 81].

The open-circuit voltage (V_{oc}) is 0.59 V (the difference in electrical potential between two terminals of a device when no external load is applied), and the fill-factor (FF) is 0.532 (the proportion of a solar (photovoltaic) cell’s actual power to its power when both current and voltage are at their maximum), as well as the power-conversion efficiency (Z) (the quantity of energy generated as a proportion of the quantity of energy used). In the case of a photovoltaic device, the ratio of electric energy generated by the device under one-sun conditions to energy incident onto the cell) of 4.85%. In [PPY-S]^{TF}-Si and [PPY-

M]^{TF}-Si devices, the fluctuation of short-circuit photocurrent (J_{sc}) with incident light intensity (P_{in}) is illustrated in Fig. 13b. The (J_{sc}) follows the power law with an exponent of 0.62, i.e., $(J_{sc} \propto P_{in})^S$. In ion processes, ($J_{sc} \propto P_{in}$)^S values of 0.5 and 1.0 correspond to bimolecular and monomolecular recombination, respectively [82]. The exponent for a continuous distribution of trapping centers is between 0.5 and 1.0. The presence of a continuous trap distribution is confirmed by the s values measured for the Au/[PPY-S]^{TF}/n-Si/Al and Au/[PPY-M]^{TF}/n-Si/Al diodes. Trap centers, according to its value, control the lifespan of photocarriers [83].

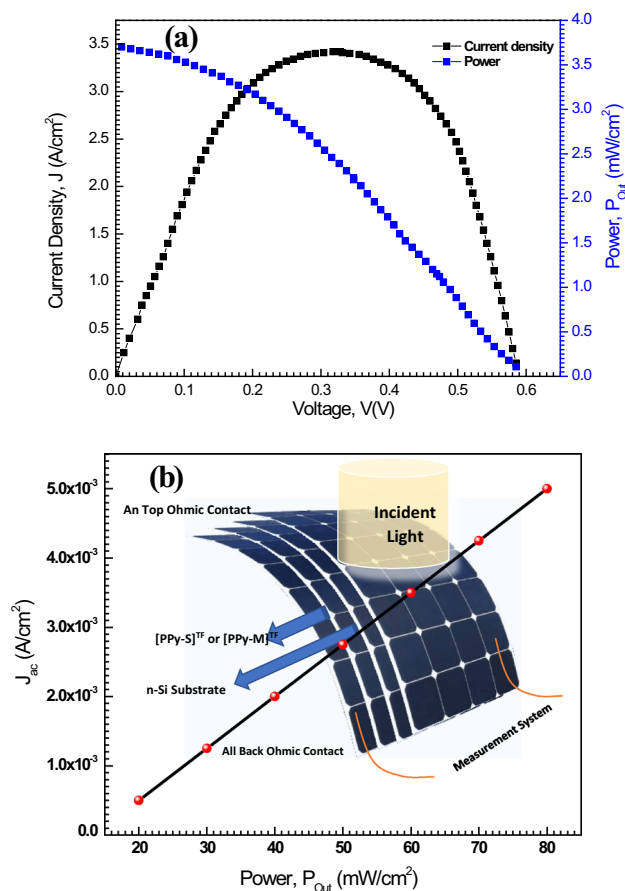


Fig. 13 **a** Current density_voltage and power_voltage characteristics. **b** Short_circuit current_power characteristics. Insert figure Schematic diagram of Au/[PPy-M]^{TF}/n-Si/Al heterojunction

4 Conclusion

Using the oxidative polymerization process in the presence of MO and SDS, one-dimensional and two-dimensional hydrochloric acid-doped polypyrrole were synthesized. The synthesis technique and testing conditions have an impact on the polypyrrole's unique properties. [PPy-S]^{TF} and [PPy-M]^{TF} thin films with a thickness (150 ± 5 nm) were fabricated using PVD method. Geometric optimization, electronic spectra, infrared spectrum and MEP of the investigated [PPY] as isolated state were performed utilizing the DFT method. The crystalline size was $D_{av} = 69.79$ nm, and it was between 39.56 and 97.25 nm. Polymorph with symmetry Triclinic in the space group $\bar{P}1$ used content studio software to calculate the theoretical X-ray diffraction models (version 7.0). The optical simulations show that polypyrrole tubes (one dimension) have a higher conductivity

than polypyrrole sheets (two dimensions). For one and two-dimensional polypyrrole, ΔE_g^{Opt} values of up to 2.88 eV and 2.15 eV were discovered. The observed Stokes shift, $\Delta = \lambda_{Emission} - \lambda_{Excitation}$, was computed as $\cong 25$ nm and 31 nm, for [PPy-S]^{TF} and [PPy-M]^{TF}, respectively. All of the fabricated thin film and solutions emitted a deep-blue light with a CIE of $y < 0.1$. Under 50 mW/cm^2 white-light lighting, the heterojunction of one-dimensional polypyrrole exhibits photovoltaic performance with an open-circuit voltage of 0.59 V, a short-circuit current density of 4.88 mA/cm^2 , a fill-factor of 0.532, and a power-conversion efficiency of 4.85%.

Acknowledgements

This project was funded by the Deanship of Scientific Research (DSR) at Applied Science Research Center Qassim University, under Grant No. (10131-cos-2020-1-3-I). The authors, therefore, acknowledge with thanks DSR for technical and financial support.

Author contributions

Conceptualization, HM, EMFAEH, NFHA. NFHA, and AFA-H; software, HM, EMFAEH, and AFAH; formal analysis, HM, EMFAEH, and AFAH; data curation, HM, and AFAH; writing-review and editing, EMFAEH, and AFAH; supervision, HM, EMFAEH, NFHA. NFHA; project administration, HM; All authors have read and agreed to the published version of the manuscript.

Funding

The funded was provided by Qassim University (Grant No. 10131-cos-2020-1-3-I).

Data availability

The data presented in this study are available in the article.

Declarations

Conflicts of interest There are no conflicts to declare.

Informed consent Not applicable.

References

1. Y. Wang, Y. Ding, X. Guo, G. Yu, Conductive polymers for stretchable supercapacitors. *Nano Res.* **12**, 1978–1987 (2019)
2. J. Stejskal, M. Trchová, Conducting polypyrrole nanotubes: a review. *Chem. Pap.* **72**, 1563–1595 (2018)
3. S. Rafique, R. Sharif, I. Rashid, S. Ghani, Facile fabrication of novel silver-polypyrrole-multiwall carbon nanotubes nanocomposite for replacement of platinum in dye-sensitized solar cell. *AIP Adv.* **6**, 085018 (2016)
4. Z. Chen, G. Zhang, W. Yang, B. Xu, Y. Chen, X. Yin, Y. Liu, Superior conducting polypyrrole anti-corrosion coating containing functionalized carbon powders for 304 stainless steel bipolar plates in proton exchange membrane fuel cells. *Chem. Eng. J.* **393**, 124675 (2020)
5. Z. Yildiz, I. Usta, A. Gungor, Electrical properties and electromagnetic shielding effectiveness of polyester yarns with polypyrrole deposition. *Text. Res. J.* **82**, 2137–2148 (2012)
6. T.F. Otero, J.G. Martinez, Physical and chemical awareness from sensing polymeric artificial muscles. *Exp. Model. Progress Polym. Sci* **44**, 62–78 (2015)
7. S. Chaudhary, A. Kiran Kumar, N.D. Sharma, M. Gupta, Cauliflower-shaped ternary nanocomposites with enhanced power and energy density for supercapacitors. *Int. J. Energy Res.* **43**, 3446–3460 (2019)
8. J. Kopecká, D. Kopecký, M. Vřňata, P. Fitl, J. Stejskal, M. Trchová, P. Bober, Z. Morávková, J. Prokeš, I. Sapurina, Polypyrrole nanotubes: mechanism of formation. *RSC Adv.* **4**, 1551–1558 (2014)
9. A. Abed-Elmageed, M.S. Zoromba, R. Hassanien, A. Al-Hossainy, Facile synthesis of spin-coated poly (4-nitroaniline) thin film: structural and optical properties. *Opt. Mater.* **109**, 110378 (2020)
10. Y. Du, H. Niu, J. Li, Y. Dou, S.Z. Shen, R. Jia, J. Xu, Morphologies tuning of polypyrrole and thermoelectric properties of polypyrrole nanowire/graphene composites. *Polymers* **10**, 1143 (2018)
11. L.-X. Wang, X.-G. Li, Y.-L. Yang, Preparation, properties and applications of polypyrroles. *React. Funct. Polym.* **47**, 125–139 (2001)
12. M. Omastova, M. Trchova, J. Kovářová, J. Stejskal, Synthesis and structural study of polypyrroles prepared in the presence of surfactants. *Synth. Met.* **138**, 447–455 (2003)
13. Y.-Z. Long, M.-M. Li, C. Gu, M. Wan, J.-L. Duvail, Z. Liu, Z. Fan, Recent advances in synthesis, physical properties and applications of conducting polymer nanotubes and nanofibers. *Prog. Polym. Sci.* **36**, 1415–1442 (2011)
14. N. Almutlaq, A. Al-Hossainy, M.S. Zoromba, Combined experimental and theoretical study, characterization, and nonlinear optical properties of doped-poly (p-nitroaniline-co-o-aminophenol) thin films. *J. Mol. Struct.* **1227**, 129712 (2021)
15. W. Zhang, L. Fu, H. Yang, Micrometer-scale mixing with pickering emulsions: biphasic reactions without stirring. *ChemSuschem* **7**, 391–396 (2014)
16. Y. Li, P. Bober, M. Trchová, J. Stejskal, Polypyrrole prepared in the presence of methyl orange and ethyl orange: nanotubes versus globules in conductivity enhancement. *J. Mater. Chem. C* **5**, 4236–4245 (2017)
17. J. Stejskal, M. Trchová, P. Bober, Z. Morávková, D. Kopecký, M. Vřňata, J. Prokeš, M. Varga, E. Watzlová, Polypyrrole salts and bases: superior conductivity of nanotubes and their stability towards the loss of conductivity by deprotonation. *RSC Adv.* **6**, 88382–88391 (2016)
18. N. Baghdadi, M.S. Zoromba, M. Abdel-Aziz, A. Al-Hossainy, M. Bassyouni, N. Salah, One-dimensional nanocomposites based on polypyrrole-carbon nanotubes and their thermoelectric performance. *Polymers* **13**, 278 (2021)
19. M. Almasoudi, M.S. Zoromba, M. Abdel-Aziz, M. Bassyouni, A. Alshahrie, A.M. Abusorrah, N. Salah, Optimization preparation of one-dimensional polypyrrole nanotubes for enhanced thermoelectric performance. *Polymer* **228**, 123950 (2021)
20. M.S. Zoromba, M. Abdel-Aziz, M. Bassyouni, A.M. Abusorrah, A. Attar, N. Baghdadi, N. Salah, Polypyrrole sheets composed of nanoparticles as a promising room temperature thermo-electric material. *Physica E Low-Dimens. Syst. Nanostruct.* **134**, 114889 (2021)
21. X. Yang, Z. Zhu, T. Dai, Y. Lu, Facile fabrication of functional polypyrrole nanotubes via a reactive self-degraded template. *Macromol. Rapid Commun.* **26**, 1736–1740 (2005)
22. H. Menon, G. Gopakumar, V. Sankaranarayanan Nair, S.V. Nair, M. Shanmugam, 2D-layered MoS₂-Incorporated TiO₂-nanofiber-based dye-sensitized solar cells. *Chem. Select* **3**, 5801–5807 (2018)
23. M.S. Zoromba, A. Al-Hossainy, M. Rzaigui, A. Abdelkader, F. Alresheedi, I. El Azab, F.M. Eissa, Facile synthesis of single-crystal of o-phenylene diamine dihydrochloride as a polychloride and fabrication of high-performance semiconductor thin film. *Opt. Mater.* **112**, 110758 (2021)
24. M.A. Chougulea, S.G. Pawara, P.R. Godsea, R.N. Mulika, S. Senb, V.B. Patila, Synthesis and characterization of polypyrrole (PPy) thin films. *Soft Nanosci. Lett.* **1**, 5 (2011)
25. J.O. Iroh, C. Williams, Formation of thermally stable polypyrrole-naphthalene/benzene sulfonate-carbon fiber composites by an electrochemical process. *Synth. Met.* **99**, 1–8 (1999)

26. M. Abdel-Aziz, E.Z. El-Ashtoukhy, M.S. Zoromba, M. Bassyouni, G. Sedahmed, Removal of nitrates from water by electrocoagulation using a cell with horizontally oriented Al serpentine tube anode. *J. Ind. Eng. Chem.* **82**, 105–112 (2020)
27. S.A. Mahmoud, A.A. Al-Dumiri, A.F. Al-Hossainy, Combined experimental and DFT-TDDFT computational studies of doped [PoDA+ PpT/ZrO₂] C nanofiber composites and its applications. *Vacuum* **182**, 109777 (2020)
28. C.-M. Seah, S.-P. Chai, S. Ichikawa, A.R. Mohamed, Control of iron nanoparticle size by manipulating PEG–ethanol colloidal solutions and spin-coating parameters for the growth of single-walled carbon nanotubes. *Particuology* **11**, 394–400 (2013)
29. M. Zwawi, A. Attar, A. Al-Hossainy, M. Abdel-Aziz, M.S. Zoromba, Polypyrrole/functionalized multi-walled carbon nanotube composite for optoelectronic device application. *Chem. Pap.* **75**, 6575–6589 (2021)
30. X. Tu, Q. Xie, C. Xiang, Y. Zhang, S. Yao, Scanning electrochemical microscopy in combination with piezoelectric quartz crystal impedance analysis for studying the growth and electrochemistry as well as microetching of poly (o-phenylenediamine) thin films. *J. Phys. Chem. B* **109**, 4053–4063 (2005)
31. A.D. Becke, Density-functional thermochemistry. I. The effect of the exchange-only gradient correction. *J. Chem. Phys.* **96**, 2155–2160 (1992)
32. C. Lee, W. Yang, R.G. Parr, Development of the Colle-Salvetti correlation-energy formula into a functional of the electron density. *Phys. Rev. B* **37**, 785 (1988)
33. G. Gaussian, 09, Revision A. 02, MJ Frisch, GW Trucks, HB Schlegel, GE Scuseria, MA Robb, JR Cheeseman, G, Scalmani, V. Barone, B. Mennucci, GA Petersson, H. Nakatsuji, M. Caricato, X. Li, HP Hratchian, AF Izmaylov, J. Bloino (2009).
34. H.K. Thabet, A. Al-Hossainy, M. Imran, Synthesis, characterization, and DFT modeling of novel organic compound thin films derived from 2-amino-4-(2-hydroxy-3-methoxyphenyl)-4H-thiazolo [3, 2-a][1, 3, 5] triazin-6 (7H)-one. *Opt. Mater.* **105**, 109915 (2020)
35. A.A. Al-Hossainy, Combined experimental and TDDFT-DFT computation, characterization, and optical properties for synthesis of keto-bromothymol blue dye thin film as optoelectronic devices. *J. Electron. Mater.* **50**, 3800–3813 (2021)
36. S.M. Ibrahim, A. Bourezgui, A. Abd-Elmageed, I. Kacem, A.F. Al-Hossainy, Structural and optical characterization of novel [ZnKCMC] TF for optoelectronic device applications. *J. Mater. Sci.: Mater. Electron.* **31**, 8690–8704 (2020)
37. J. Kopecká, M. Mrlík, R. Olejník, D. Kopecký, M. Vřnata, J. Prokeš, P. Bober, Z. Morávková, M. Trchová, J. Stejskal, Polypyrrole nanotubes and their carbonized analogs: synthesis, characterization, gas sensing properties. *Sensors* **16**, 1917 (2016)
38. D. Kopecký, M. Varga, J. Prokeš, M. Vřnata, M. Trchová, J. Kopecká, M. Václavík, Optimization routes for high electrical conductivity of polypyrrole nanotubes prepared in presence of methyl orange. *Synth. Met.* **230**, 89–96 (2017)
39. D. Wolff, A. Demangeon (1872–1940) Sources et bibliographie, *Cybergeo Eur. J. Geogr.* (2005). <https://doi.org/10.4000/cybergeo.5493>
40. A. Ibrahim, M. Abdel-Aziz, M.S. Zoromba, A. Al-Hossainy, Structural, optical, and electrical properties of multi-walled carbon nanotubes/polyaniline/Fe₃O₄ ternary nanocomposites thin film. *Synth. Met.* **238**, 1–13 (2018)
41. F. Akman, Experimental and theoretical investigation of molecular structure, vibrational analysis, chemical reactivity, electrostatic potential of benzyl methacrylate monomer and homopolymer. *Can. J. Phys.* **94**, 853–864 (2016)
42. A. Al-Hossainy, H.K. Thabet, M.S. Zoromba, A. Ibrahim, Facile synthesis and fabrication of a poly (ortho-anthranilic acid) emeraldine salt thin film for solar cell applications. *New J. Chem.* **42**, 10386–10395 (2018)
43. L. Liu, L. Miao, L. Li, F. Li, Y. Lu, Z. Shang, J. Chen, Molecular electrostatic potential: a new tool to predict the lithiation process of organic battery materials. *J. Phys. Chem. Lett.* **9**, 3573–3579 (2018)
44. M.S. Zoromba, A. Al-Hossainy, M. Abdel-Aziz, Conductive thin films based on poly (aniline-co-o-anthranilic acid)/magnetite nanocomposite for photovoltaic applications. *Synth. Met.* **231**, 34–43 (2017)
45. C. Suresh, A. Bai Amutha, F. Sayyed, Correlation and prediction of redox potentials of hydrogen evolution mononuclear cobalt catalysts via molecular electrostatic potential: a DFT study. *J. Phys. Chem. A* **120**, 1112–1119 (2016)
46. R.K. Shah, K.S. Abou-Melha, F.A. Saad, T. Yousef, G.A. Al-Hazmi, M.G. Elghalban, A.M. Khedr, N. El-Metwaly, Elaborated studies on nano-sized homo-binuclear Mn (II), Fe (III), Co (II), Ni (II), and Cu (II) complexes derived from N2O2 Schiff base, thermal, molecular modeling, drug-likeness, and spectral. *J. Therm. Anal. Calorim.* **123**, 731–743 (2016)
47. V. Choudhary, A. Bhatt, D. Dash, N. Sharma, DFT calculations on molecular structures, HOMO–LUMO study, reactivity descriptors and spectral analyses of newly synthesized diorganotin (IV) 2-chloridophenylacetohydroxamate complexes. *J. Comput. Chem.* **40**, 2354–2363 (2019)
48. A. Al-Hossainy, M.S. Zoromba, M. Abdel-Aziz, M. Bassyouni, A. Attar, M. Zwawi, A. Abd-Elmageed, H. Maddah, A.B. Slimane, Fabrication of heterojunction diode using doped-poly (ortho-aminophenol) for solar cells applications. *Physica B* **566**, 6–16 (2019)

49. A. Al-Hossainy, M. Bassyouni, M.S. Zoromba, Elucidation of electrical and optical parameters of poly (o-anthranilic acid)-poly (o-amino phenol)/copper oxide nanocomposites thin films. *J. Inorg. Organomet. Polym. Mater.* **28**, 2572–2583 (2018)
50. I. Kacem, M. Daoudi, W. Dridi, H. Sellemi, K. Harzli, G. De Izzara, B. Geslot, H. Guermazi, P. Blaise, F. Hosni, Effects of neutron–gamma radiation on the free radical contents in epoxy resin: upconversion luminescence and structural stabilization. *Appl. Phys. A* **125**, 1–9 (2019)
51. R. Srivastava, L. Sinha, M. Karabacak, O. Prasad, S. Pathak, A. Asiri, M. Cinar, Spectral features, electric properties, NBO analysis and reactivity descriptors of 2-(2-Benzothiazolylthio)-Ethanol: combined experimental and DFT studies. *Spectrochim. Acta Part A Mol. Biomol. Spectrosc.* **136**, 1205–1215 (2015)
52. N. Almutlaq, A. Al-Hossainy, Novel synthesis, structure characterization, DFT and investigation of the optical properties of diphenylphosphine compound/zinc oxide [DPPB+ ZnO] C nanocomposite thin film. *Compos. Interfaces* **28**, 879–904 (2021)
53. M. Nabati, E. Pournamdari, Y. Dashti-Rahmatabadi, S. Sarsar, Withaferin A (WIT) Interaction with beta–tubulin to promote tubulin degradation: in Silico study. *Adv. J. Chem. B* **2**, 26–32 (2020)
54. A.F. Al-Hossainy, A. Ibrahim, Synthesis, structural and optical properties of novel 3-(3, 5-dimethyl-1H-pyrazol-1-yl)-1-(diphenylphosphino)-2-((diphenylphosphino) methyl)-3-methylbutanone-1, 2-diphenylethane-1, 2-diamine tungsten dicarbonyl (PyrPMB-W) nanostructure thin film. *Opt. Mater.* **46**, 131–140 (2015)
55. A.F. Al-Hossainy, R.M. Abdelaal, W.N. El Sayed, Novel synthesis, structure characterization, DFT and investigation of the optical properties of cyanine dye/zinc oxide [4-CHMQI/ ZnO] C nanocomposite thin film. *J. Mol. Struct.* **1224**, 128989 (2021)
56. I. Hotovy, J. Huran, P. Siciliano, S. Capone, L. Spiess, V. Rehacek, The influences of preparation parameters on NiO thin film properties for gas-sensing application. *Sens. Actuators B Chem.* **78**, 126–132 (2001)
57. B.-H. Jeong, E.M. Hoek, Y. Yan, A. Subramani, X. Huang, G. Hurwitz, A.K. Ghosh, A. Jawor, Interfacial polymerization of thin film nanocomposites: a new concept for reverse osmosis membranes. *J. Membr. Sci.* **294**, 1–7 (2007)
58. A. Łukowiak, R. Dylewicz, S. Patela, W. Stręk, K. Maruszewski, Optical properties of SiO₂–TiO₂ thin film waveguides obtained by the sol–gel method and their applications for sensing purposes. *Opt. Mater.* **27**, 1501–1505 (2005)
59. M.S. Zoromba, M. Bassyouni, M. Abdel-Aziz, A.F. Al-Hossainy, N. Salah, A. Al-Ghamdi, M.R. Eid, Structure and photoluminescence characteristics of mixed nickel–chromium oxides nanostructures. *Appl. Phys. A* **125**, 1–10 (2019)
60. A. Al-Hossainy, M.S. Zoromba, O. El-Gammal, F.I. El-Dosoki, Density functional theory for investigation of optical and spectroscopic properties of zinc-quinonoid complexes as semiconductor materials. *Struct. Chem.* **30**, 1365–1380 (2019)
61. T. Lindgren, J.M. Mwabora, E. Avendano, J. Jonsson, A. Hoel, C.-G. Granqvist, S.-E. Lindquist, Photoelectrochemical and optical properties of nitrogen doped titanium dioxide films prepared by reactive DC magnetron sputtering. *J. Phys. Chem. B* **107**, 5709–5716 (2003)
62. H. Mansour, A.E. Halium, M. Eman, N.F. Alrasheedi, M.S. Zoromba, A.F. Al-Hossainy, Combined experimental and TDDFT computational studies of the optical and electrical characteristic of luminol films-doped TiO₂ with 9.027% power conversion efficiency. *J. Mater. Sci.: Mater. Electron.* **33**, 5244 (2022)
63. M.S. Zoromba, M. Abdel-Aziz, M. Bassyouni, A. Attar, A. Al-Hossainy, Synthesis and characterization of Poly (ortho-aminophenol-co-para-toluidine) and its application as semiconductor thin film. *J. Mol. Struct.* **1225**, 129131 (2021)
64. K. Sanadi, P. Sanadi, M. Gaur, A. Mali, G. Kamble, Optical, electrical and morphological studies of βHgS thin film prepared by improved chemical bath deposition technique. *Bull. Mater. Sci.* **44**, 1–5 (2021)
65. M. Abdel-Aziz, M.S. Zoromba, M. Bassyouni, M. Zwawi, A. Alshehri, A. Al-Hossainy, Synthesis and characterization of Co-Al mixed oxide nanoparticles via thermal decomposition route of layered double hydroxide. *J. Mol. Struct.* **1206**, 127679 (2020)
66. M.H. Abdel-Aziz, E.Z. El-Ashtoukhy, M. Bassyouni, A.F. Al-Hossainy, E.M. Fawzy, S. Abdel-Hamid, M.S. Zoromba, DFT and experimental study on adsorption of dyes on activated carbon prepared from apple leaves. *Carbon Lett.* **31**, 863–878 (2021)
67. S. Kaya, B. Tüzün, C. Kaya, I.B. Obot, Determination of corrosion inhibition effects of amino acids: quantum chemical and molecular dynamic simulation study. *J. Taiwan Inst. Chem. Eng.* **58**, 528–535 (2016)
68. S. Kaya, L. Guo, C. Kaya, B. Tüzün, I. Obot, R. Touir, N. Islam, Quantum chemical and molecular dynamic simulation studies for the prediction of inhibition efficiencies of some piperidine derivatives on the corrosion of iron. *J. Taiwan Inst. Chem. Eng.* **65**, 522–529 (2016)
69. S.M. Ibrahim, A. Bourezgui, A.F. Al-Hossainy, Novel synthesis, DFT and investigation of the optical and electrical properties of carboxymethyl cellulose/thiobarbituric acid/copper oxide [CMC+ TBA/CuO] C nanocomposite film. *J. Polym. Res.* **27**, 1–18 (2020)

70. A. Ibrahim, A. Al-Hossainy, Thickness dependence of structural and optical properties of novel 2-((1, 1-bis (diphenylphosphino)-2-phenylpropan-2-yl)-chromium tetracarbonyl-amino)-3-phenylpropanoic acid copper (II)(DPP-Cr-Palan-Cu) nanocrystalline thin film. *Synth. Met.* **209**, 389–398 (2015)
71. M.S. Zoromba, M. Tashkandi, A. Alshehri, M. Abdel-Aziz, M. Bassyouni, S. Mahmoud, A.B. Slimane, A. Al-Hossainy, Polymer solar cell based on doped o-anthranilic acid and o-aminophenol copolymer. *Opt. Mater.* **104**, 109947 (2020)
72. A. Al-Hossainy, A. Ibrahim, Facile synthesis, X ray single crystal and optical characterizations of Cu-diphenylphosphino-methane organic crystalline semi-conductors. *J. Optoelectron. Adv. Mater.* **16**, 1472–1480 (2014)
73. K. Sasaki, T. Nagamura, Ultrafast all-optical switch using complex refractive index changes of thin films containing photochromic dye. *Appl. Phys. Lett.* **71**, 434–436 (1997)
74. T.J. Alwan, Gamma irradiation effect on the optical properties and refractive index dispersion of dye doped polystyrene films. *Turk. J. Phys.* **36**, 377–384 (2012)
75. S.M. Ibrahim, A.F. Al-Hossainy, Synthesis, structural characterization, DFT, kinetics and mechanism of oxidation of bromothymol blue: application to textile industrial wastewater treatment. *Chem. Pap.* **75**, 297–309 (2021)
76. N. Madadi Mahani, First-principles calculations on photocatalytic activity of ZnWO₄ doped with Lithium. *Medbiotech J.* **5**, 37–40 (2021)
77. S. Amir-Al-Zumahi, N. Arobi, M.M. Rahman, M.K. Hossain, M.A.J. Rozy, M. Bashar, A. Amri, H. Kabir, M.A. Hossain, F. Ahmed, Understanding the optical behaviours and the power conversion efficiency of novel organic dye and nanostructured TiO₂ based integrated DSSCs. *Sol. Energy* **225**, 129–147 (2021)
78. Z.N. Kayani, S. Rahim, R. Sagheer, S. Riaz, S. Naseem, Assessment of antibacterial and optical features of sol-gel dip coated La doped TiO₂ thin films. *Mater. Chem. Phys.* **250**, 123217 (2020)
79. K.I. Aly, M.M. Sayed, M.G. Mohamed, S.W. Kuo, O. Younis, A facile synthetic route and dual function of network luminescent porous polyester and copolyester containing porphyrin moiety for metal ions sensor and dyes adsorption. *Microporous Mesoporous Mater.* **298**, 110063 (2020)
80. K.C. Rathod, K.R. Sanadi, P.D. Kamble, G.S. Kamble, M.L. Gaur, K.M. Garadkar, Photovoltaic solar application study of Cu 0.5 Zn 0.5 Se thin films by chemical bath deposition method. *Mater. Res.* (2022). <https://doi.org/10.1590/1980-5373-mr-2021-0259>
81. K.C. Rathod, Synthesis characterization of copper selenide thin films and study of photovoltaic solar applications. *Mater. Sci. Ind. J.* **19**, 157 (2021)
82. H. Feng, N. Qiu, X. Wang, Y. Wang, B. Kan, X. Wan, M. Zhang, A. Xia, C. Li, F. Liu, An ADA type small-molecule electron acceptor with end-extended conjugation for high performance organic solar cells. *Chem. Mater.* **29**, 7908–7917 (2017)
83. K.C. Rathod, P.D. Kamble, K.R. Sanadi, G.S. Kamble, M.L. Guar, K.M. Garadkar, Photovoltaic application study of zinc telluride thin films grown by chemical bath deposition method. *Adv. Mater. Phys. Chem.* **11**, 131–144 (2021)

Publisher's Note Springer Nature remains neutral with regard to jurisdictional claims in published maps and institutional affiliations.